



# Formulation of Stiffness and Strength Characteristics of Flexible Wire Ropes and Their Application in Photovoltaic Support Structures

Chuangju Zhang<sup>\*</sup>, Leige Xu<sup>†</sup>, Pengshuai Liu<sup>‡</sup>

School of Civil Engineering and Transportation, North China University of Water Resources and Electric Power, 450045 Zhengzhou, China

<sup>\*</sup> Correspondence: Chuangju Zhang (zhangchuangju@stu.ncwu.edu.cn)

Received: 04-18-2024

Revised: 06-15-2024

Accepted: 06-23-2024

**Citation:** C. J. Zhang, L. G. Xu, and P. S. Liu, “Formulation of stiffness and strength characteristics of flexible wire ropes and their application in photovoltaic support structures,” *Precis. Mech. Digit. Fabr.*, vol. 1, no. 2, pp. 66–74, 2024. <https://doi.org/10.56578/pmdf010202>.



© 2024 by the author(s). Published by Acadlore Publishing Services Limited, Hong Kong. This article is available for free download and can be reused and cited, provided that the original published version is credited, under the CC BY 4.0 license.

**Abstract:** The safety and functionality of flexible photovoltaic (PV) racking systems critically depend on understanding the force and deformation behavior of wire ropes. This study establishes mechanical equilibrium equations to derive the deformation curve, maximum displacement, and maximum tension of wire ropes subjected to loading. Analytical dimensionless equations indicate that variations in the orientation of PV modules do not affect the structural stiffness or forces exerted on the wire ropes. Engineering calculations of maximum displacement and tension are compared with results from finite element simulations, revealing less than a 1% discrepancy between the analytical and numerical outcomes. Analysis of characteristic parameter curves in relation to prestress demonstrates that the maximum deflection span ratio decreases as prestress increases, while the maximum tensile stress rises with increasing prestress. The proposed formulas are validated as both accurate and practical, effectively reflecting the changes in wire rope forces with varying prestress levels. This study provides valuable insights for the mechanical analysis and structural design of flexible PV mounting systems, offering a robust reference for future engineering applications.

**Keywords:** Flexible photovoltaic (PV) support; Wire rope; Force analysis; Prestress; Deflection span ratio

## 1 Introduction

Solar energy represents a clean and renewable source of power, essential for achieving sustainable development goals [1, 2]. PV modules can generate electricity from solar energy [3, 4]. To ensure the safe and efficient operation of PV power generation systems, the design of racking systems with substantial spans and effective load-bearing capacities is critical. Although research on traditional rigid PV mounting systems is well-established [5–8], such systems are limited by their small span and inability to adapt to complex terrains. In contrast, flexible PV mounts, which utilize prestressed steel cables, can span larger distances and adjust to varying terrain conditions without requiring extensive support structures [9–11]. Steel cables make effective use of the mechanical properties of the material [12], which have been widely applied in bridge structures [13, 14].

By applying prestress to the steel wire ropes, flexible PV brackets can enhance load distribution and improve stiffness. To fully utilize the wire rope's strength while ensuring the safety and reliability of the structural system, it is crucial to understand the force characteristics of the wire ropes. The force behavior of wire ropes is inherently nonlinear, influenced by various factors such as prestress, rope length, and other parameters. Accurate formula derivation for calculating the structural safety of flexible PV brackets is therefore of significant importance.

Previous studies have contributed to the understanding of wire rope mechanics and PV mounting systems. Aly and Bitsuamlak [15] systematically investigated the sensitivity of ground-mounted solar photovoltaic panels to wind loads through wind tunnel tests. He et al. [16, 17] introduced a new flexible PV racking system and assessed its load-bearing capacity under various loads, including self-weight, wind, and snow loads. Kim et al. [18] investigated the impact of different panel shapes on wind-induced vibrations of flexible PV mounts through wind tunnel tests. Zhang et al. [19] analyzed the aerodynamic instability characteristics of single-axis solar trackers, revealing differences in wind-induced torsional vibrations at various inclination angles. Ceferino and Lin [20] proposed a probabilistic framework to predict the power generation performance of solar infrastructure during hurricanes. Liu et al. [21]

investigated the wind response of flexible PV mounting structures through wind tunnel tests and found that changing the module size affects the aerodynamic characteristics and structural frequency of the structure, which in turn affects the wind vibration of the structure. Despite these advancements, the impact of prestress magnitude on the characteristic parameters of wire ropes remains underexplored.

This study aims to address this gap by establishing mechanical equilibrium equations for wire ropes and deriving the deflection curve equations, considering the wire rope cross-section angle. Relationships between variables such as the deflection-to-span ratio and internal forces post-deformation are explored in relation to prestress force. Example analyses reveal that stiffness and strength conditions in the support system are interrelated and sometimes contradictory. The formulas proposed in this study aim to resolve these contradictions, ensuring both structural safety and economic efficiency. The findings provide a valuable reference for the static analysis and structural design of flexible PV support systems.

## 2 Derivation of Formula

### 2.1 Wire Rope Deformation Curve Equation

The wire rope is subjected to the gravity, snow load, and wind load of the solar module. As the distance between the panels is very close, if the gap is ignored, the external force on the wire rope is simplified to a uniform load, which includes the self-weight of the wire rope. The force sketch of the wire rope is shown in Figure 1.

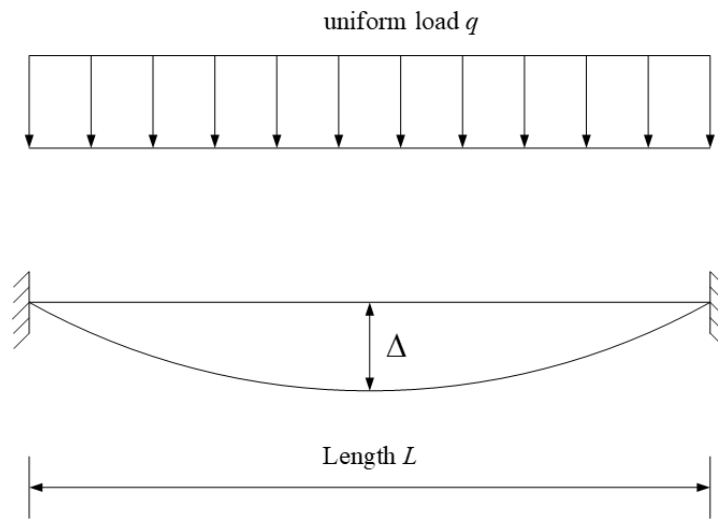


**Figure 1.** Deformation of prestressed wire rope subjected to uniform load  $q$

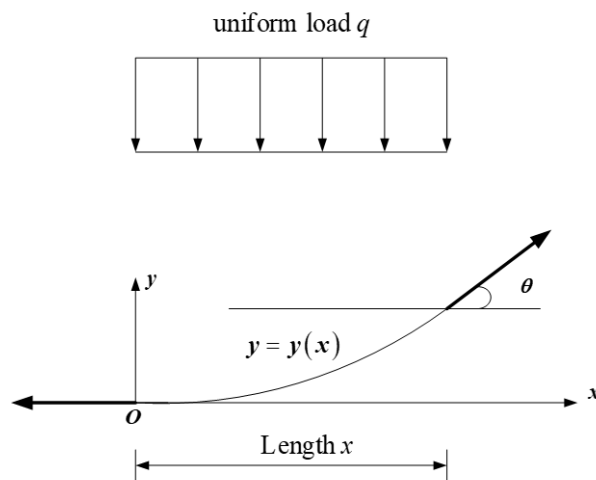


**Figure 2.** Rope force sketch

The wire rope suspended between the two columns of the curve can be expressed by mathematical equations. Assuming that the wire rope is a flexible rope that can only be subjected to tension and cannot withstand bending action, the deformation curve of the wire rope after being subjected to force is deduced. The effect of geometric nonlinearity should be considered in the analysis of cable structures. After the deformation of the midpoint of the wire rope as the origin to establish a coordinate system, take the x-axis from 0 to x of a section of the isolation body. The force is shown in Figure 2.

The deformation of the wire rope in both the vertical and horizontal directions, under the combined force, is zero.

$$T \sin \theta = qx, \quad T \cos \theta = T_0 \quad (1)$$

where,  $T$  is the tension,  $\theta$  is the angle between the wire rope cross-section normal and the horizontal plane,  $q$  is the uniform load,  $x$  is the length of the wire rope, and  $T_0$  is the tension value at the midpoint of the wire rope span.

By comparing the above two equations, the slope of the wire at any point can be determined:

$$\tan \theta = \frac{dy}{dx} = \frac{qx}{T_0} \quad (2)$$

Using differential calculus, the derivative at any point on the curve represents the tangent slope. The equation above represents the differential equation for the wire rope deformation curve. By integrating this equation over the endpoints, the deformation curve can be determined.

$$y = C_0 + \frac{q}{2T_0} x^2 \quad (3)$$

Let  $C_0$  be the integration constant. According to Figure 2 and the coordinate system construction, where  $x = 0$  when  $y = 0$ , substituting these values yields  $C_0 = 0$ . Consequently, the deformation curve of the wire rope is given by:

$$y = \frac{q}{2T_0} x^2 \quad (4)$$

As the midpoint tension value  $T_0$  increases, the displacement  $y$  decreases, indicating an inverse relationship between the two. In the coordinate system established in this study, the maximum displacement of the wire rope occurs at  $x=L/2$ . Therefore, there are:

$$y_{\max} = \frac{qL^2}{8T_0} \quad (5)$$

From Eqs. (1) and (2), we can get:

$$T(x) = \frac{T_0}{\cos \theta} = \frac{T_0}{\cos \left[ \arctan \left( \frac{qx}{T_0} \right) \right]} \quad (6)$$

Tension  $T$  reaches its maximum at  $x=L/2$ , indicating that there is:

$$T_{\max} = \frac{T_0}{\cos \left[ \arctan \left( \frac{qL}{2T_0} \right) \right]} \quad (7)$$

Tension  $T$  reaches its minimum at  $x = 0$ , and there is:

$$T_{\min} = T_0 \quad (8)$$

The strain in the wire rope at the cross-section  $x$  is given by:

$$\varepsilon(x) = \frac{T(x)}{EA} = \frac{T_0}{EA \cos \left[ \arctan \left( \frac{qx}{T_0} \right) \right]} \quad (9)$$

where  $E$  is the modulus of elasticity of the wire rope and  $A$  is the cross-sectional area. From the above equation, the total elongation of the wire rope, which includes both the elongation caused by the prestress force and the additional load  $q$ , is given by:

$$\Delta L = \int_{-L/2}^{L/2} \varepsilon(x) dx = \int_{-L/2}^{L/2} \frac{T_0}{EA \cos \left[ \arctan \left( \frac{qx}{T_0} \right) \right]} dx \quad (10)$$

The length of the curve after deformation of the wire rope is:

$$S = \int_{-L/2}^{L/2} \sqrt{1 + \tan^2 \theta} dx = \int_{-L/2}^{L/2} \sqrt{1 + \left(\frac{qx}{T_0}\right)^2} dx \quad (11)$$

It can be seen that the elongation of the wire rope due to the load  $q$  is  $S-L$ , and the elongation of the curve due to prestress is  $\Delta L - (S - L)$ , so the prestress is:

$$\sigma_{\text{initial}} = E \frac{\Delta L - (S - L)}{L} \quad (12)$$

As the temperature increases, the wire rope expands, resulting in a negative equivalent prestress. It is necessary to ensure that the maximum temperature rise still satisfies the stiffness conditions. Conversely, when the temperature decreases, the wire rope contracts, leading to a positive equivalent prestress. The design must ensure that the maximum temperature drop continues to meet the strength conditions. If the structure undergoes deformation due to a temperature rise of  $\Delta T$  from its installation state, and the corresponding coefficient of linear expansion is  $\alpha$ , then the equivalent prestress force to be added is given by:

$$\sigma_{eq} = -E\alpha\Delta T \quad (13)$$

## 2.2 Dimensionless

Flexible racking systems can be configured to place solar modules either longitudinally or horizontally, corresponding to long-span and short-span solutions, respectively. To assess the advantages and disadvantages of these two span lengths, it is essential to theoretically examine how span length affects the key design control parameters. For ease of analysis, each formula derived from the above calculations has been made dimensionless.

Let  $\Delta = y/L$ , by substituting it into Eq. (5), we get:

$$\Delta_{\text{max}} = \frac{qL}{8T_0} \quad (14)$$

The above formula represents the maximum deflection-to-span ratio for the wire rope, which characterizes the deformation stiffness of the wire rope. To satisfy the stiffness conditions, it is necessary to ensure that:

$$\Delta_{\text{max}} \leq \Delta_{\text{allow}} \quad (15)$$

where,  $\Delta_{\text{allow}}$  is the permissible deflection ratio, which is 1/30 in this case.

Let  $\eta = x/L$ , by substituting it into Eqs. (10)-(11), we get:

$$\Delta L = L \int_{-1/2}^{1/2} \frac{T_0}{EA \cos \left[ \arctan \left( \frac{qL}{T_0} \eta \right) \right]} d\eta \quad (16)$$

$$S = L \int_{-1/2}^{1/2} \sqrt{1 + \left( \frac{qL}{T_0} \eta \right)^2} d\eta \quad (17)$$

Substituting Eqs. (18) and (19) into Eq. (14) yields:

$$\sigma_{\text{initial}} = E \left[ \int_{-1/2}^{1/2} \frac{T_0}{EA \cos \left[ \arctan \left( \frac{qL}{T_0} \eta \right) \right]} d\eta - \left( \int_{-1/2}^{1/2} \sqrt{1 + \left( \frac{qL}{T_0} \eta \right)^2} d\eta - 1 \right) \right] \quad (18)$$

From the above equation, when the cross-section area  $A$  and the sum of loads  $qL$  remain constant, the initial stress  $\sigma_{\text{initial}}$  is a single-valued function of the minimum tension  $T_0$  after deformation. Similarly, Eq. (14) shows that the wire rope stiffness value is a function of the sum of loads  $qL$  and minimum tension  $T_0$ . When  $qL$  remains constant, the stiffness value is a single-valued function of the minimum tension  $T_0$ . Therefore, it can be seen that when the cross-sectional area  $A$  and the sum of the loads  $qL$  remain constant, the stiffness value  $\Delta_{\text{max}}$  is a function of the initial stress  $\sigma_{\text{initial}}$ .

The two span lengths differ only in the direction of placement of the solar modules, and the sum of the loads  $qL$  remains constant. Therefore, when the cross-sectional area  $A$  is constant, the stiffness value  $\Delta_{\text{max}}$  is a function of the initial stress  $\sigma_{\text{initial}}$ , independent of the span length.

Similarly, nondimensionalizing Eqs. (2) and (6) yields:

$$\tan \theta = \frac{qL}{T_0} \eta \quad (19)$$

$$T(\eta) = \frac{T_0}{\cos \left( \arctan \frac{qL}{T_0} \eta \right)} \quad (20)$$

From the above two equations, it can be seen that for both span lengths, since  $qL$  is the same, when the cross-sectional area  $A$  is unchanged, at any  $\eta$ -coordinate point, the turning angle  $\theta$  and the tension  $T$  are only functions of  $T_0$ . And because  $T_0$  is a univariate function of the initial stress  $\sigma_{\text{initial}}$  at this time, the corner  $\theta$  and tension  $T$  are univariate functions of the initial stress  $\sigma_{\text{initial}}$ . That is, when the initial stress  $\sigma_{\text{initial}}$  is determined, for both span lengths, the values of angle and tension at the span end ( $\eta = \pm 1/2$ ) are equal. For example, if the starting stress for both span lengths is the same, the wire rope's force on the end column is the same, so the anchorage and end column strength requirements are the same at the same prestress value. The two arrangements may have different force characteristics and instability modes under wind vibration forces.

Note that the change in cross-sectional area  $A$  is not considered in the derivation of this section, and the conclusions apply only to the case where the cross-sectional area  $A$  is consistent. After changing the crosssection, it is necessary to recalculate the structural displacements for the case of different initial prestresses.

### 3 Formula Validation

During the derivation of the theoretical solution, the external force acting on the wire rope was simplified to a uniform load, which may introduce some error. To verify the accuracy of the derived theoretical equations and to determine the potential error range, this section compares and analyzes the theoretical solution against the numerical solution obtained from ABAQUS.

#### 3.1 Algorithm

In the example, the flexible bracket has two spans, one span is 21.04 m long, the wire rope cross-sectional area is 70.88 mm<sup>2</sup>, the modulus of elasticity is 1.95×10<sup>11</sup> Pa, the prestress force is 1638 MPa, the wire rope and the PV module's self-weight equivalent mean force is 66.9 N/m, and the self-weight + snow load equivalent mean force is 520.3 N/m. Calculate the maximum displacement and maximum tensile force of the wire rope in the PV module under the action of the module's self-weight and after snowing. Calculate the maximum displacement and maximum tension of the single-span wire rope under the self-weight of the PV module and after snowfall.

#### 3.2 Static Calculation

(1) Considering only the wire rope and the self-weight of the PV module  $q = 66.9$  N/m

$$\sigma_{\text{initial}} = E \frac{\int_{-L/2}^{L/2} \frac{T_0}{EA \cos \left[ \arctan \left( \frac{66.9x}{T_0} \right) \right]} dx - \left( \int_{-L/2}^{L/2} \sqrt{1 + \left( \frac{66.9x}{T_0} \right)^2} dx - L \right)}{L} = 1.638 \times 10^9 \text{ N/m}^2 \quad (21)$$

By substituting  $E$ ,  $A$ , and  $L$  into the above equation and performing integration using MATLAB software, the solution  $T_0 = 116185$  N is obtained:

$$y_{\text{max}} = \frac{66.9 \times 21.04^2}{8 \times 116185} = 0.0319 \text{ m} \quad (22)$$

$$T_{\text{max}} = \frac{116185}{\cos \left[ \arctan \left( \frac{66.9 \times 21.04}{2 \times 116185} \right) \right]} = 116187 \text{ N} \quad (23)$$

(2) Considering self-weight + snow load  $q = 520.3$  N/m, solve for  $T_0 = 120789$  N

$$y_{\text{max}} = \frac{520.3 \times 21.04^2}{8 \times 120788} = 0.2384 \text{ m} \quad (24)$$

$$T_{\text{max}} = \frac{120788}{\cos \left[ \arctan \left( \frac{520.3 \times 21.04}{2 \times 120788} \right) \right]} = 120913 \text{ N} \quad (25)$$

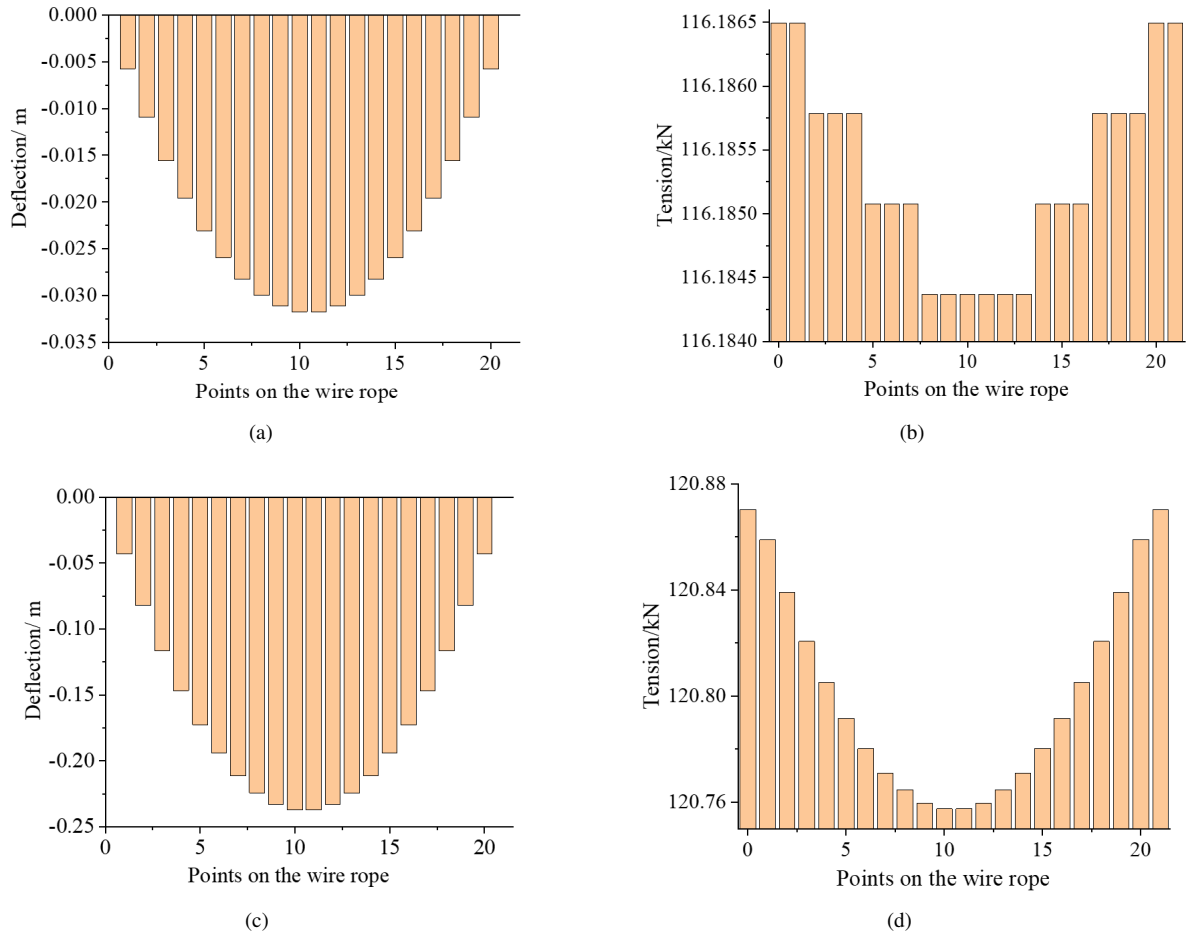


**Figure 3.** ABAQUS calculation results: (a)  $q=66.9$  N/m, Wire rope deflection; (b)  $q=66.9$  N/m, Wire rope tension; (c)  $q=520.3$  N/m, Wire rope deflection; (d)  $q=520.3$  N/m, Wire rope tension

**Table 1.** Comparison with finite element calculation results

Prestress/MPa			Formula Solution	Numerical Solution	Discrepancy
1638	$y_{\max}$ /m	$q = 66.9$ N/m	0.03186	0.03170	0.50%
		$q = 520.3$ N/m	0.23836	0.23729	0.45%
	$T_{\max}$ /N	$q = 66.9$ N/m	116187	116180	0.01%
		$q = 520.3$ N/m	120913	120870	0.04%
1404	$y_{\max}$ /m	$q = 66.9$ N/m	0.03716	0.03696	0.54%
		$q = 520.3$ N/m	0.27251	0.27129	0.45%
	$T_{\max}$ /N	$q = 66.9$ N/m	99637	99631	0.01%
		$q = 520.3$ N/m	105791	105737	0.05%
1170	$y_{\max}$ /m	$q = 66.9$ N/m	0.04455	0.04429	0.59%
		$q = 520.3$ N/m	0.31578	0.31441	0.44%
	$T_{\max}$ /N	$q = 66.9$ N/m	83099	83095	0.01%
		$q = 520.3$ N/m	91337	91269	0.07%
936	$y_{\max}$ /m	$q = 66.9$ N/m	0.05558	0.05521	0.67%
		$q = 520.3$ N/m	0.37053	0.36891	0.44%
	$T_{\max}$ /N	$q = 66.9$ N/m	66603	66600	0.01%
		$q = 520.3$ N/m	77894	77802	0.12%

### 3.3 Comparative Analysis of Theoretical and Numerical Solutions

In this section, a model was created in ABAQUS, with concentrated loads of 66.9 N and 520.3 N applied at equal intervals of 1 meter. The theoretical solutions obtained from the derived equations were compared with the results

from ABAQUS to evaluate the error introduced by the simplification to a uniform load.

Truss elements were used for modeling the wire rope, with three translational displacements and axial rotations constrained at both ends. Geometric nonlinearity was incorporated into the calculation model, although the effects of deformation and displacement at the span ends and columns were excluded. The coefficient of linear expansion of the wire rope was set at  $1.2 \times 10^{-5}/^{\circ}\text{C}$ , and a prestressing force of 1638 MPa was applied to the wire rope using the “cooling method.” The finite element analysis provided the deflection and tension at the upper point of the wire rope, as illustrated in Figure 3 (the transverse axis represents points on the wire rope at 1-meter intervals).

Table 1 presents the errors between the theoretical and numerical solutions for various wire rope prestresses. The maximum error observed between the theoretical solutions and the finite element results for the maximum displacement and tension of the wire rope is less than 1%. This indicates that the simplifications applied to the theoretical formula are scientifically and reasonably justified, allowing for continued study based on the derived theoretical formula.

#### 4 Variation of Characteristic Parameters with Prestress

The key characteristic parameters are the deflection-to-span ratio and the maximum tensile stress of the wire rope. Prestress plays a crucial role in ensuring the structural safety, and analyzing how these characteristic parameters vary with prestress under a uniform load of 520.3 N/m can provide valuable insights for engineering applications.

##### 4.1 Maximum Deflection Ratio

Figure 4 illustrates that the maximum deflection-to-span ratio of the wire rope decreases as the prestress increases. Initially, the reduction in the deflection-to-span ratio is more pronounced, but as prestress continues to increase, this reduction becomes less significant, indicating a clear nonlinear relationship. Specifically, the maximum deflection-to-span ratios of the wire rope were 0.0334, 0.0277, 0.0122, and 0.0104 for prestress values of 0 MPa, 300 MPa, 1500 MPa, and 1800 MPa, respectively. The deflection-to-span ratio decreased by 0.0057 as prestress increased from 0 MPa to 300 MPa, and by 0.0018 when prestress increased from 1500 MPa to 1800 MPa. The rate of decrease was notably reduced, with the average reduction rate dropping to approximately 0.32 times that observed in the initial stage.

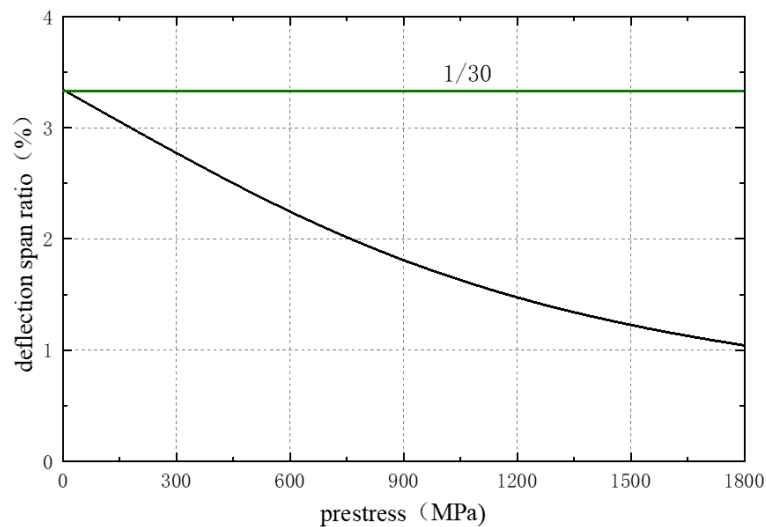


**Figure 4.** Variation curve of wire rope deflection span ratio with prestress

##### 4.2 Maximum Stress

According to Figure 5, the maximum tension of the wire rope in each working condition reaches the strength limit required to ensure structural safety. The curve indicates that the maximum stress increases slowly at first, but the rate of increase accelerates with higher prestress. Specifically, the maximum stress values of the wire rope were 583 MPa, 701 MPa, 1579 MPa, and 1857 MPa for prestress levels of 0 MPa, 300 MPa, 1500 MPa, and 1800 MPa, respectively. The maximum stress increased by 118 MPa when the prestress rose from 300 MPa to 600 MPa and by 278 MPa when it increased from 1500 MPa to 1800 MPa, reflecting a significant rise. The average increase rate of maximum stress increased to approximately 2.36 times that observed in the initial stage.

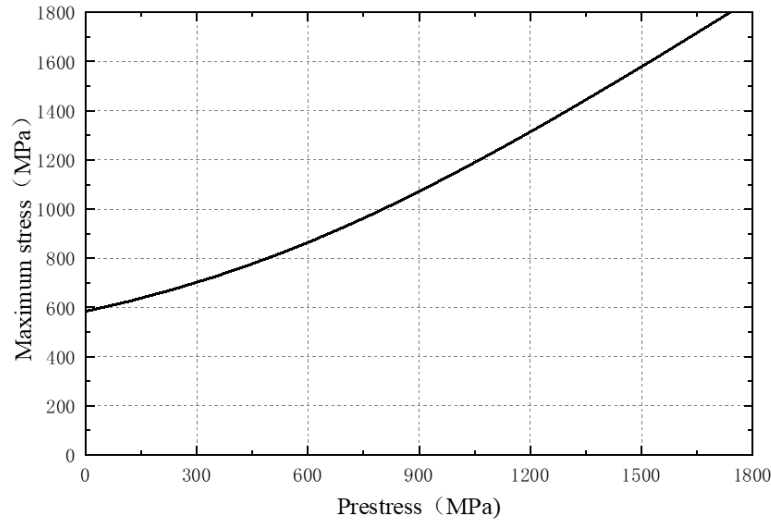


**Figure 5.** Variation curve of maximum stress with prestress

## 5 Conclusions

(1) The deformed wire rope was investigated, and a coordinate system was established to account for the cross-sectional angle after deformation. Mechanical equilibrium equations were formulated to derive expressions for the maximum displacement and maximum tensile force. The theoretical solutions for these parameters, as calculated from the derived formulas, exhibit a maximum deviation of less than 1% compared to the numerical solutions obtained from finite element analysis. This confirms that the derived formulas, based on the simplifications employed, are scientifically sound and reliable for practical applications.

(2) Theoretical analyses reveal that, when comparing long-span and short-span schemes with identical wire rope diameters and permissible deflection-span ratios, both schemes require equivalent prestress and the same force on the end columns. Thus, under identical strength and stiffness conditions, the choice between long-span and short-span schemes should be guided by the specific characteristics and constraints of the site. It should be noted that while these conclusions are based on static calculations, the impact of dynamic forces such as wind-induced vibrations on force characteristics and instability modes warrants further investigation.

(3)  $\Delta_{\max} = qL/8T_0$  represents the formula for the maximum deflection-to-span ratio of the wire rope, which characterizes the deformation stiffness. This formula is utilized to ascertain whether the wire rope meets the required stiffness criteria.  $T_{\max} = T_0/\cos[\arctan(qL/2T_0)]$  is used to calculate the maximum tension in the wire rope, thereby determining its compliance with strength requirements. The prestress value  $T_0$  can be identified by substituting the relevant parameters from Eqs. (10) and (11) into Eq. (12).

(4) Analysis of the characteristic parameters as functions of wire rope prestress reveals that, beyond a certain prestress value, the rate of decrease in the maximum deflection-to-span ratio diminishes, while the rate of increase in maximum tension accelerates. The curves indicate that the minimum prestress value required to satisfy both stiffness and strength criteria can be identified. This insight aids in optimizing construction costs while ensuring structural safety and provides valuable guidance for the static analysis and design of similar engineering applications.

## Data Availability

The data used to support the research findings are available from the corresponding author upon request.

## Conflicts of Interest

The authors declare no conflict of interest.

## References

- [1] J. Q. Liu, S. Y. Li, J. Luo, and Z. Q. Chen, "Experimental study on critical wind velocity of a 33-meter-span flexible photovoltaic support structure and its mitigation," *J. Wind Eng. Ind. Aerodyn.*, vol. 236, p. 105355, 2023. <https://doi.org/10.1016/j.jweia.2023.105355>
- [2] S. M. Choi, C. D. Park, S. H. Cho, and B. J. Lim, "Effects of wind loads on the solar panel array of a floating photovoltaic system-Experimental study and economic analysis," *Energy*, vol. 256, p. 124649, 2022. <https://doi.org/10.1016/j.energy.2022.124649>



- [3] A. R. Wittwer, J. M. Podestá, H. G. Castro, J. L. Mroginski, J. O. Marighetti, M. E. De Bortoli, R. R. Paz, and F. Mateo, "Wind loading and its effects on photovoltaic modules: An experimental-Computational study to assess the stress on structures," *Sol. Energy*, vol. 240, pp. 315–328, 2022. <https://doi.org/10.1016/j.solener.2022.04.061>
- [4] A. Bahadori and C. Nwaoha, "A review on solar energy utilisation in Australia," *Renew. Sustain. Energy Rev.*, vol. 18, pp. 1–5, 2013. <https://doi.org/10.1016/j.rser.2012.10.003>
- [5] A. Abiola-Ogedengbe, H. Hangan, and K. Siddiqui, "Experimental investigation of wind effects on a standalone photovoltaic (PV) module," *Renew. Energy*, vol. 78, pp. 657–665, 2015. <https://doi.org/10.1016/j.renene.2015.01.037>
- [6] C. M. Jubayer and H. Hangan, "Numerical simulation of wind effects on a stand-alone ground mounted photovoltaic (PV) system," *J. Wind Eng. Ind. Aerodyn.*, vol. 134, pp. 56–64, 2014. <https://doi.org/10.1016/j.jweia.2014.08.008>
- [7] C. M. Jubayer and H. Hangan, "A numerical approach to the investigation of wind loading on an array of ground mounted solar photovoltaic (PV) panels," *J. Wind Eng. Ind. Aerodyn.*, vol. 153, pp. 60–70, 2016. <https://doi.org/10.1016/j.jweia.2016.03.009>
- [8] A. Agarwal, H. Irtaza, and M. J. Ahmad, "Numerical analysis of the ground-mounted solar PV panel array mounting systems subjected to basic wind for optimum design," *Can. J. Civ. Eng.*, vol. 48, no. 6, pp. 656–668, 2021. <https://doi.org/10.1139/cjee-2019-0280>
- [9] Y. F. Zhu, Y. Huang, C. Z. Xu, B. Xiao, C. H. Chen, and Y. Yao, "Effect of tilt angle on wind-induced vibration in pre-stressed flexible cable-supported photovoltaic systems," *Sol. Energy*, vol. 277, p. 112729, 2024. <https://doi.org/10.1016/j.solener.2024.112729>
- [10] Y. C. Kim, Y. Tamura, A. Yoshida, T. Ito, W. Shan, and Q. Yang, "Experimental investigation of aerodynamic vibrations of solar wing system," *Adv. Struct. Eng.*, vol. 21, no. 15, pp. 2217–2226, 2018. <https://doi.org/10.1177/1369433218770799>
- [11] S. Y. Li, J. Ma, J. Q. Liu, and Z. Q. Chen, "Experimental study for flutter performance of flexible photovoltaic system by segmental model test," *China Civ. Eng. J.*, vol. 57, no. 2, pp. 25–34, 2024. <https://doi.org/10.15951/j.tmgcxb.22111107>
- [12] A. S. K. Bendalla and G. Morgenthal, "A nonlinear finite element framework for static and dynamic analysis of structural cables with deviating supports," *Eng. Struct.*, vol. 291, p. 116363, 2023. <https://doi.org/10.1016/j.engstruct.2023.116363>
- [13] H. Zhang, H. Wang, Z. D. Xu, Z. Q. Liu, and H. Gao, "Dynamic performance of ultra-long stay cable in small-scale extreme winds," *Eng. Struct.*, vol. 290, p. 116369, 2023. <https://doi.org/10.1016/j.engstruct.2023.116369>
- [14] S. B. Chai, Q. Wu, and X. L. Wang, "Deformation and force characteristics of double-cable suspension bridges," *Structures*, vol. 54, pp. 1705–1716, 2023. <https://doi.org/10.1016/j.istruc.2023.05.102>
- [15] A. M. Aly and G. Bitsuamlak, "Aerodynamics of ground-mounted solar panels: Test model scale effects," *J. Wind Eng. Ind. Aerodyn.*, vol. 123, pp. 250–260, 2013. <http://doi.org/10.1016/j.jweia.2013.07.007>
- [16] X. H. He, H. Ding, H. Q. Jing, F. Zhang, X. P. Wu, and X. J. Weng, "Wind-induced vibration and its suppression of photovoltaic modules supported by suspension cables," *J. Wind Eng. Ind. Aerodyn.*, vol. 206, p. 104275, 2020. <https://doi.org/10.1016/j.jweia.2020.104275>
- [17] X. H. He, H. Ding, H. Q. Jing, X. P. Wu, and X. J. Weng, "Mechanical characteristics of a new type of cable-supported photovoltaic module system," *Sol. Energy*, vol. 226, pp. 408–420, 2021. <https://doi.org/10.1016/j.solener.2021.08.065>
- [18] Y. C. Kim, W. Shan, Q. S. Yang, Y. Tamura, A. Yoshida, and T. Ito, "Effect of panel shapes on wind-induced vibrations of solar wing system under various wind environments," *J. Struct. Eng.*, vol. 146, no. 6, p. 04020104, 2020. [https://doi.org/10.1061/\(ASCE\)ST.1943-541X.0002642](https://doi.org/10.1061/(ASCE)ST.1943-541X.0002642)
- [19] X. B. Zhang, W. Y. Ma, X. H. Kang, Q. J. Shao, and Z. Q. Tang, "Experimental study of the torsional aeroelastic instability of single-axis solar trackers under different turbulence intensities," *J. Wind Eng. Ind. Aerodyn.*, vol. 240, p. 105486, 2023. <https://doi.org/10.1016/j.jweia.2023.105486>
- [20] L. Ceferino and N. Lin, "Hurricane risk of solar generation in the United States," *Nat. Hazards Rev.*, vol. 24, no. 4, p. 04023029, 2023. <https://doi.org/10.1061/NHREFO.NHENG-1764>
- [21] J. Q. Liu, S. Y. Li, and Z. Q. Chen, "Experimental study on effect factors of wind-induced response of flexible photovoltaic support structure," *Ocean Eng.*, vol. 307, p. 118199, 2024. <https://doi.org/10.1016/j.oceaneng.2024.118199>